2021

Microstructure evolution and mechanical property response of TC11 titanium alloy under electroshock treatment

Chang Liu

Lechun Xie

Dongsheng Qian

Lin Hua

Liqiang Wang

See next page for additional authors

10.1016/j.matdes.2020.109322
Liu, C., Xie, L., Qian, D., Hua, L., Wang, L., & Zhang, L. C. (2021). Microstructure evolution and mechanical property response of TC11 titanium alloy under electroshock treatment. *Materials & Design, 198*, article 109322.
https://doi.org/10.1016/j.matdes.2020.109322

Materials and Design 198 (2021) 109322

Contents lists available at ScienceDirect

Materials and Design

journal homepage: www.elsevier.com/locate/matdes

Microstructure evolution and mechanical property response of TC11 titanium alloy under electroshock treatment

Chang Liu [a,b], Lechun Xie [a,b,*], Dongsheng Qian [c], Lin Hua [a,b,*], Liqiang Wang [d,*], Lai-Chang Zhang [e]

[a] Hubei Key Laboratory of Advanced Technology for Automotive Components, Wuhan University of Technology, Wuhan 430070, PR China
[b] Hubei Collaborative Innovation Center for Automotive Components Technology, Wuhan 430070, PR China
[c] School of Materials Science and Engineering, Wuhan University of Technology, Wuhan 430070, PR China
[d] State Key Laboratory of Metal Matrix Composites, School of Materials Science and Engineering, Shanghai Jiao Tong University, No. 800 Dongchuan Road, Shanghai 200240, PR China
[e] School of Engineering, Edith Cowan University, 270 Joondalup Drive, Joondalup, Perth, WA 6027, Australia

HIGHLIGHTS

- Plenty of fine needlelike α martensite (α_M) were precipitated after EST by 0.06 s.
- The yield strength was increased from 959 MPa to 1265 MPa after EST by 0.06 s.
- The average hardness was increased from 358 HV to 396 HV after EST by 0.06 s.
- The fracture mode was transformed from plastic/brittle fracture to brittle fracture.
- Above results caused by α_M precipitates and the weave structures with dislocations.

GRAPHICAL ABSTRACT

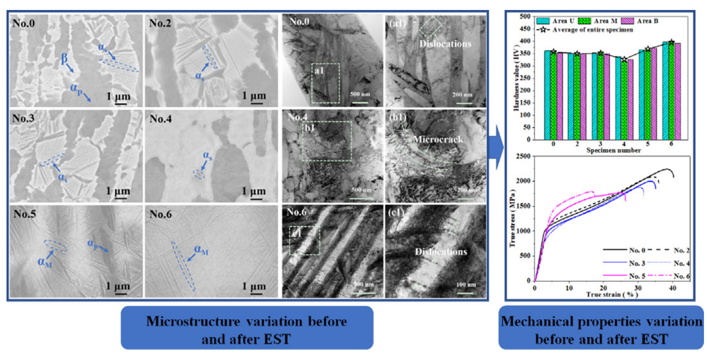

ARTICLE INFO

Article history:
Received 9 July 2020
Received in revised form 15 October 2020
Accepted 9 November 2020
Available online 11 November 2020

Keywords:
Electroshock treatment (EST)
Microstructure
Mechanical properties
Phase transition
Titanium alloy

ABSTRACT

This work investigated the effects of electroshock treatment (EST) on the microstructure variation and mechanical properties of TC11 alloy. The average hardness of the specimens decreased from 358 HV to 328 HV after EST of 0.04 s, then increased to 396 HV after EST of 0.06 s. After EST, the yield strength of specimen declined from 959 MPa to 797 MPa after EST of 0.04 s, and then increased to 1265 MPa after EST of 0.06 s, but the fracture strain decreased continuously. The variation in mechanical properties was closely related to the phase transition from the secondary α (α_s) to β phase, and the precipitation of refined needlelike α martensite (α_M). The diffusion of atoms accompanied by broaden α_s/β boundary from 11.2 nm to 27.6 nm due to the phase transformation after EST by 0.04 s and the dislocation pileup at the boundary to form defects, which resulted the decrease in strength. While increasing the EST time to 0.06 s, the width of α_M/β boundary decreased to 5.91 nm. All results indicated that the EST is an effective method for optimizing the microstructure and mechanical properties of titanium alloys in a short time.

1. Introduction

Titanium alloys are widely used in aerospace, marine and medical [1–7], and other fields due to their excellent properties such as high specific strength, good corrosion resistance and low density, high heat

* Corresponding authors.
E-mail addresses: xielechun@whut.edu.cn (L. Xie), hualin@whut.edu.cn (L. Hua), wang_liqiang@sjtu.edu.cn (L. Wang).

https://doi.org/10.1016/j.matdes.2020.109322

Table 1
EST time and the number of specimens.

Specimen number	EST time
No.0	Untreated
No.2	0.02 s
No.3	0.03 s
No.4	0.04 s
No.5	0.05 s
No.6	0.06 s

resistance and strength, etc. [8–13]. Among titanium alloys, TC11 with a nominal composition of Ti-6.5Al-1.5Zr-3.5Mo-0.3Si is a typical two-phase titanium alloy, and it is mainly applied in the manufacture of compressor discs, blades and other parts in the aerospace because of its high service temperature of 500 °C [14–18]. It is known that the mechanical properties of TC11 alloy are closely dependent on the microstructure, which can be tailored according to different service requirements through various processing methods. Tailoring the mechanical properties of TC11 alloy plays an important role both in the aerospace and the industrial applications.

Some researchers have put sight in the effect of different treatments on mechanical properties of TC11 alloy. Song et al. [19] found that TC11 alloy with lamellar structures consisting of α/β lamellae or acicular α' martensite laths had a higher fatigue crack initiation threshold from the notch at different cooling rates from the β transition temperature. Ibrahim et al. [20] revealed that the optimal combination of hardness, tensile properties, and wear resistance of TC11 alloy was achieved after heat treating at 1050 °C with fine lamellar structure. Huang et al. [21] found that a good combination of tensile strength (990 MPa) and elongation (12.8%) had been obtained by hot compression at 995 °C followed by a duplex annealing treatment. Gu et al. [22] discovered the specimen after heat treatment (970 °C/1 h/AC (cool in air) + 530 °C/6 h/AC) showed the best creep performance in the study of heat treatment on the tensile creep behavior of duplex TC11 over the temperature range of 450–550 °C and the stress range of 300–450 MPa. In these studies, although the heat treatment can optimize the microstructure of TC11, the high-temperature and long-time treatment, and the specific conditions had been required sometimes, such as the high pressure, vacuum, and so on. Therefore, simple, energy-saving and rapid methods for manipulating microstructure are very important to the development of titanium alloys.

Electrical pulse treatment has attracted the attention of researchers in recent years. Wang et al. [23] revealed that the nano-size voids around carbides in cold rolled M50 bearing steel had been extensively healed after electropulsing treatment. Gao et al. [24] indicated that the electric current pulse could restrain the growth of the dendrite in ZA27 alloy and enhance the tensile strength and the elongation. Huo et al. [25] showed that the fracture strain of the EPH-treated specimen of Ti6441 alloys was obviously increased from 23% to 29% by dynamic compression test, owing to the attenuation of local stress concentration, and the fracture strength retained a fairly high level. Wang et al. [26] found a maximum improvement in microhardness of Cu–Cr–Zr alloy of about 20 HV was observed at a current density of 0.35 A/mm2, and the softening temperature of the alloy was delayed for about 50–75 °C. Liao et al. [27] reflected that very fine macrostructure was obtained by applying an electric current pulse during the nucleation of the melt in structure of pure aluminum. Levitin et al. [28] found the fatigue resistance of titanium alloy increased by a strong current pulse treatment, and the surface residual stresses and electric resistance of specimens were decreased.

Compared with electric pulse treatment, electroshock treatment (EST) shows more advantages, the higher current energy and density, and the continuous and stable pulse current for processing components flexibility. Xie et al. [29] found that acicular secondary α transformed to β phase in TC11 alloy after EST. Xie et al. [30] found that refined subgrains were precipitated in the large columnar β grains in near-β titanium alloy manufactured by directed energy deposition and the α phase precipitated along the grain boundary tended to grow after EST, the curvature radius of the α tips increased and distinct spheroidization occurred. Wu et al. [31] found that the phase structure of Ti-6.6Al-3.4Mo alloy changed after EST, and the phase structure variation caused the change of hardness. Song et al. [32] studied the change of residual stress in cold rolled M50 steel under EST, and the residual stress after treatment was reduced and distributed evenly, and the elongation was evidently improved with no loss of yield strength. Compared to heat treatments, EST is a simple and energy-saving method, which does not require severe environmental conditions and can improve the mechanical properties of titanium alloy by the rapid phase transformation.

Therefore, the advantages of EST are applied to optimize the microstructure and mechanical properties of TC11 alloy, with aim to provide new ideas and methods for processing titanium alloy. In this work, the TC11 alloy was treated by EST with different parameters, and the mechanical properties including the hardness and compression test were evaluated. The microstructure evolution was characterized and analyzed by scanning electron microscopy (SEM) and transmission electron microscopy (TEM) before and after EST. Thus, the influence mechanism

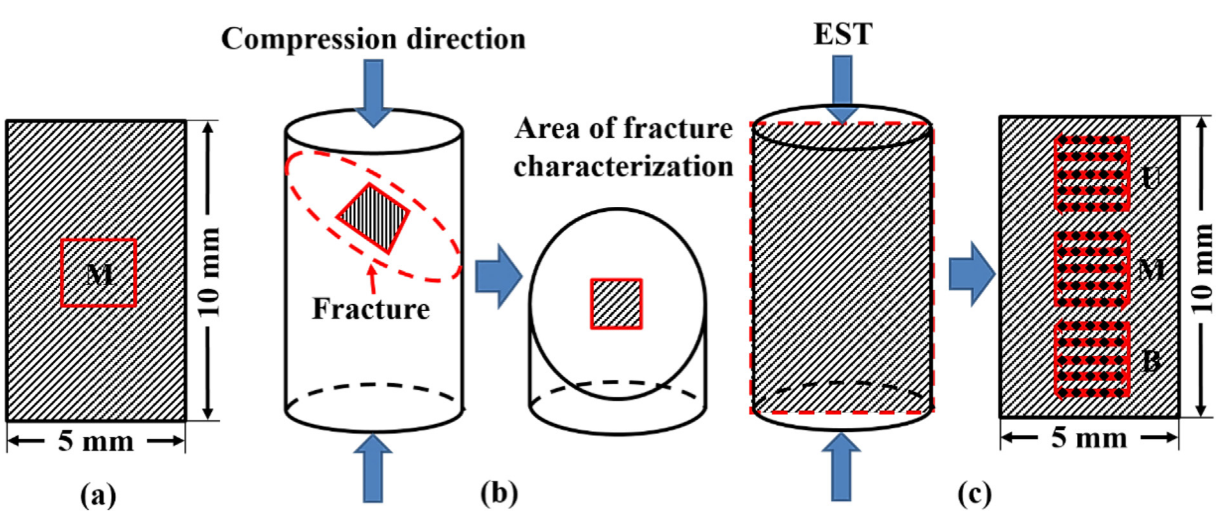

Fig. 1. Characterization areas for (a) microstructure, (b) the fracture surface after compression, and (c) the specimens after hardness tests.

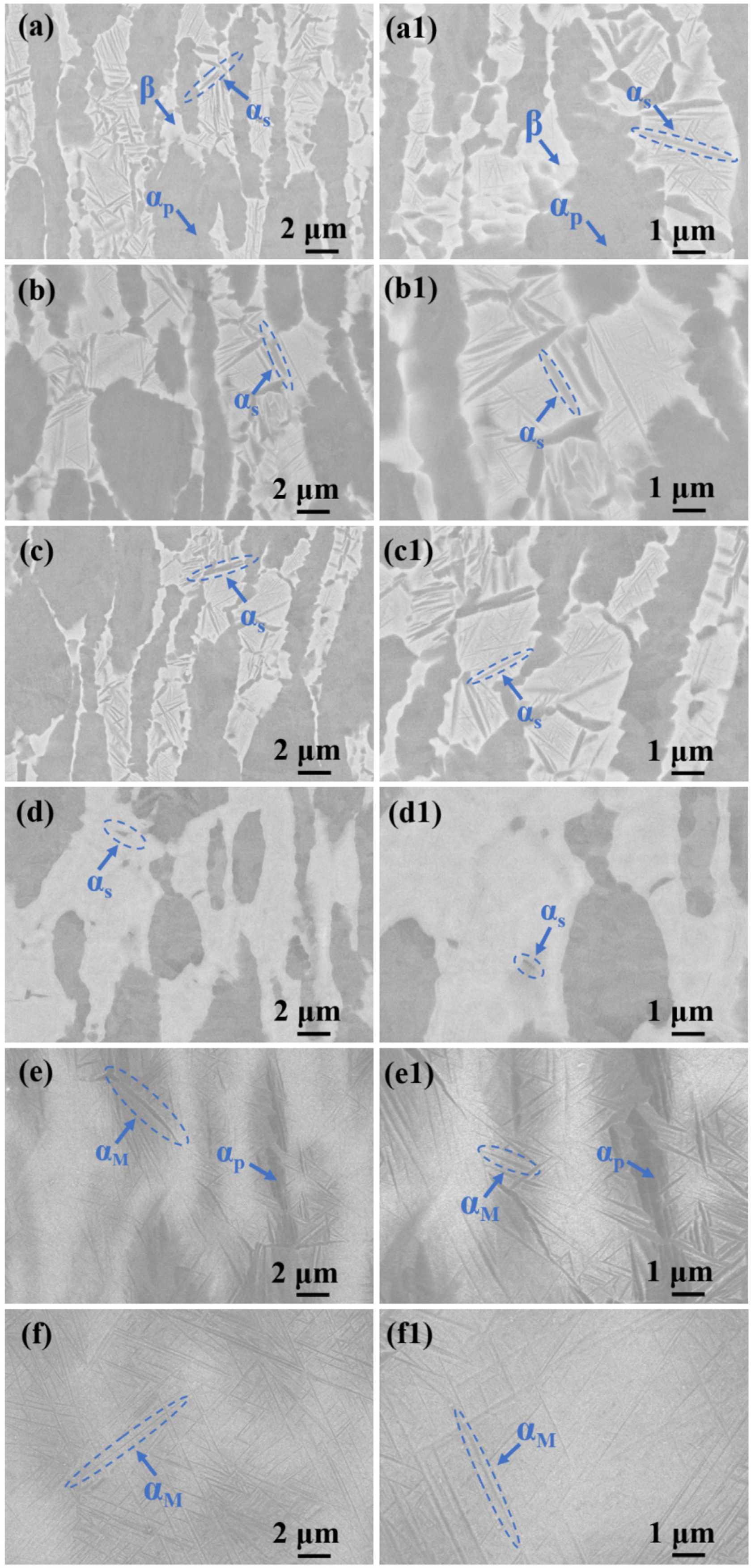

Fig. 2. Phase structure of specimens: (a) (a1), (b) (b1), (c) (c1), (d) (d1), (e) (e1), and (f) (f1) represent No.0, No.2, No.3, No.4, No.5 and No.6 respectively with low and high magnification.

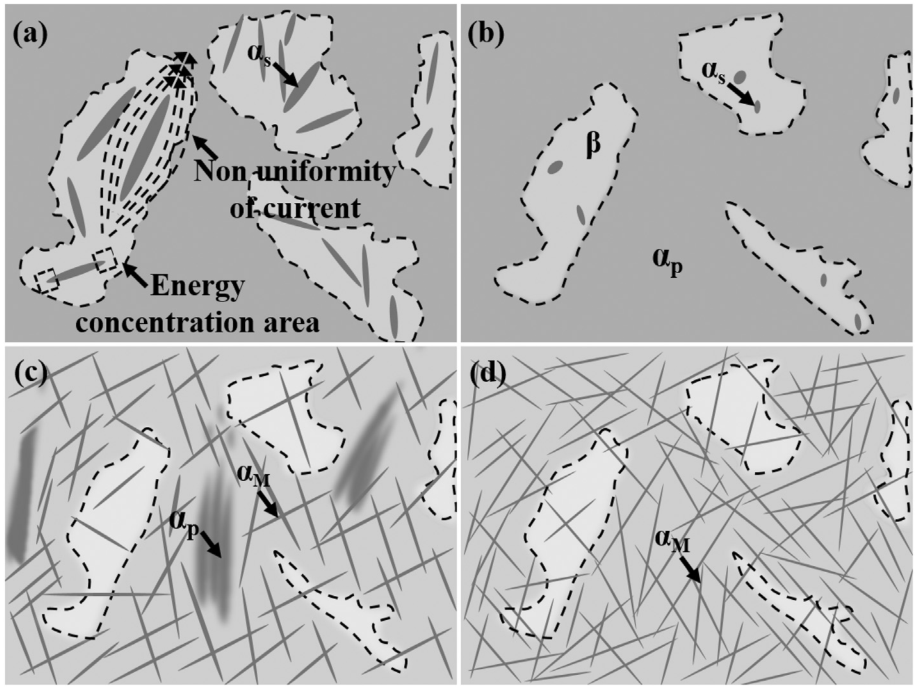

Fig. 3. Schematic diagram of variation of the acicular α_s phase and the needlelike α_M by different EST time: (a), (b), (c) and (d) represent No.0, No.4, No.5 and No.6 respectively.

of mechanical properties was explored according to the microstructure variation, and the relation between them was discussed in detail.

2. Experimental

2.1. Specimens preparation and EST

The TC11 alloy was obtained from Baoji Titanium Industry Co., Ltd. (China). Cylindrical specimens with 5 mm in diameter and 10 mm in length were machined from the raw rod material by wire-electrode cutting. After machining, the surface oxide layer was removed by abrasive papers. Afterward, the specimens were treated by EST with different time. The schematic diagram of EST and the specimen preparation can be found in reference [33]. The current amplitude of EST through the specimens was 4200 A and the corresponding current density was

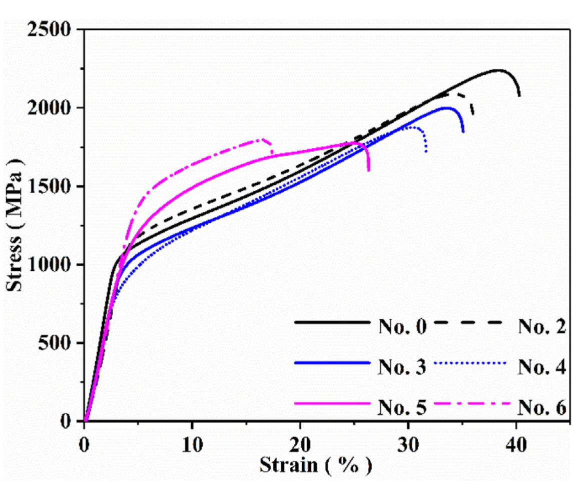

Fig. 4. Compressive true stress - strain curves of specimens No.0, No.2, No.3, No.4, No.5 and No.6.

213.9 A/mm^2. The EST time and the number of specimens were shown in Table 1.

2.2. Microstructure characterization

SEM and TEM were utilized to characterize the microstructure variation in the middle area (M) of specimens (shown in Fig. 1(a)). The specimens were cut along the central axis of the cylinders, and prepared by the standard metallographic methods and ground by abrasive papers successively up to 4000 grits, then polished using the solution of OPS (a suspension of SiO_2) and H_2O_2 mixed with the ratio of 3: 2. After polishing, the specimens were cleaned by the ultrasonic method in ethanol for 8 mins. SEM (Zeiss, Germany) was utilized to characterize and analyze the variation in phase structure under a voltage of 10 kV. The characterization area M (shown in Fig. 1) was selected for TEM observation. The specimens for TEM observation were prepared by grinding and plasma thinning. The thickness of specimen was grinded to 100 μm using 4000 grit abrasive paper, and then set different angles to carry out ion thinning on the sample until holes appear. The dislocations on grain boundaries and the element distribution were characterized and analyzed by Talos F200S TEM (FEI, America). The electron gun acceleration voltage was 200 kV, the minimum spot beam size was 0.3 nm, the TEM point resolution was 0.25 nm, and the information resolution was 0.12 nm.

2.3. Mechanical testing

The compression experiments were carried out on SANS-CMT5205 testing machine with a compression rate of 0.05 mm/min at room temperature. The compressive stress-strain curves were obtained in accordance with the standard GB / T 7314–2005 test and the loading directions of compression were shown in Fig. 1(b). The fracture morphology was characterized by SEM, and the middle area of the fracture morphology was selected to study the fracture mechanism (shown in Fig. 1(b)).

The Vickers hardness of specimens before and after EST were tested by HUAYIN HV-1000A (China) in the upper (U), middle

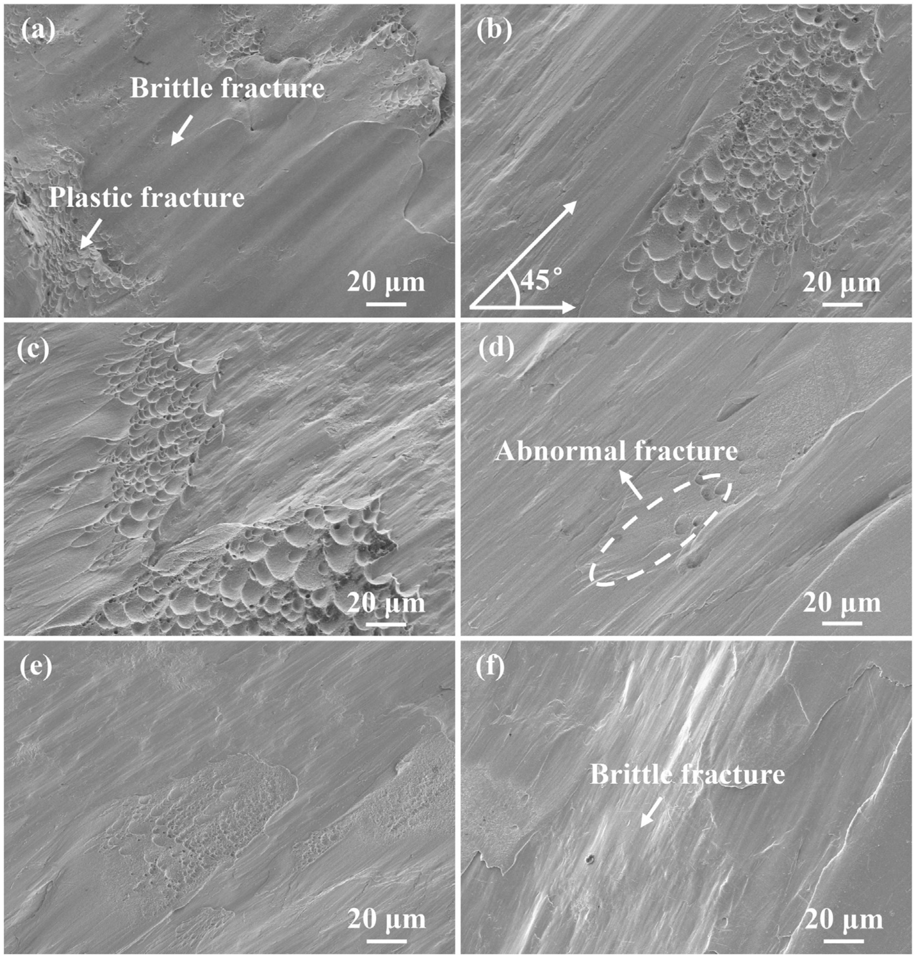

Fig. 5. Fracture morphology of compressed specimens: (a) No. 0, (b) No. 2, (c) No. 3, (d) No. 4, (e) No. 5 and (f) No. 6.

(M) and bottom (B) positions, respectively, as shown in Fig. 1(c). Before hardness testing, the measurement areas of the specimen were polished. The measurement of 25 points with 5 × 5 square matrix was adopted in order to measure the hardness accurately, and the schematic of points were shown in Fig. 1(c). The distance between each matrix was 1 mm, and the spacing between two adjacent points was 0.5 mm. The applied load was 500 N, and the holding time was 5 s. The statistics of hardness in each area could show the variation of hardness in detail.

3. Results and discussion

3.1. Evolution of phase structure

The phase structure in specimens before and after EST are shown in Fig. 2. The white and gray areas represent the β and primary α (α_p) phases respectively, and the secondary α (α_s) phases are dispersed in the β phase before EST (shown in Fig. 2(a) and (a1)). Fig. 2(b), (b1) and Fig. 2(c), (c1) show the phase structure of the specimens after EST of 0.02 s and 0.03 s, respectively. The phase variation is not evident after EST of 0.02 s and 0.03 s, which is similar to those shown in Fig. 2(a) and (a1). However, the significant difference can be observed in Fig. 2(d) and (d1); acicular α_s originally existed in β phase is transformed to β phase after EST of 0.04 s, and the acicular α_s phases passivate into a short rod and finally transforms into β phase. With further increasing the EST time, the different phase transition appears in Fig. 2(e), (e1) and (f), (f1). Massive fine needlelike α martensite (α_M) appear in the α_p and β phase and the original phase boundaries of α_p and β phase are not distinct in Fig. 2(e) and (e1). While increasing the EST time, the temperature rises sharply in a short time (resulting in the temperature over that of β phase transition), after cooling in the air, the fine needlelike α_M is precipitated [33]. Moreover, the needlelike α_M precipitates in No. 6 are smaller and more uniformly distributed compared to those in No. 5, which is ascribed to the higher temperature introduced by EST with different time. The needlelike α_M is mainly distributed in the area of α_p phase. But the incomplete precipitation of α_M in No.5 and the complete precipitation of α_M in No.6 can be observed in Fig. 2(e), (e1) and (f), (f1).

Before EST, the phase constituents consist of the α_p, β, and the acicular α_s phase. The primary interfaces of α_p/β show the jagged morphology and the interfaces are not smooth (in Fig. 2(a) and (a1)). The acicular α_s phase can be equivalent to an ellipse, and a plenty of the tips of ellipses are accumulated on the α_p/β interface and squeeze the interface, and the jagged interfaces are formed. Comparing with Fig. 2(a) and (a1), the jagged morphology of the α_p/β interfaces in Fig. 2(d) and (d1) become smoother after EST of 0.04 s, which is mainly related to the phase transition of the acicular α_s to β phase. The phase transition results in the spheroidization of acicular α_s and the tips of them become smoother after EST of 0.04 s. The evolution of phase structure would influence the mechanical properties, which is further investigated.

The schematic of the phase transition after EST is shown in Fig. 3. During EST, the heat generated at the tips of the acicular α_s causes the temperature to reach the phase transition temperature of $\alpha \rightarrow \beta$ instantaneously. The temperature on tips of acicular α_s rises immediately and decreases, leading to the local phase transition of

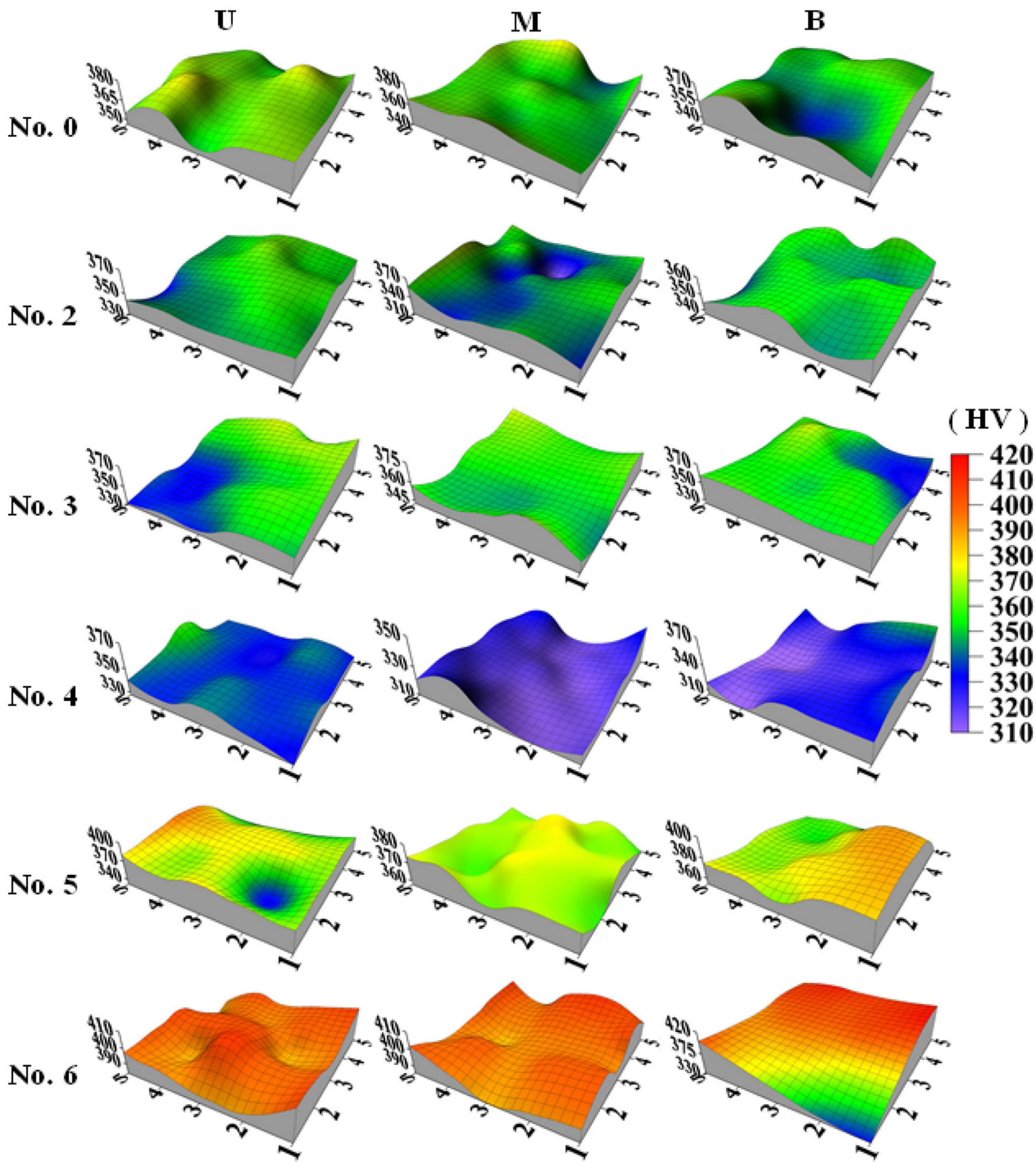

Fig. 6. Three-dimensional contour of hardness distribution of specimens.

tips and edges of α_s phase, and the passivation of the tips of acicular α_s phase is a sign of the phase transition. It indicates the thermal effect [34,35] of EST in Fig. 3(a). In addition, the currents flowing through the α_s and β phases under the same EST parameter are different due to the difference in resistivity between the α_s and β phases, forming the non-thermal effect, which accelerates the atom diffusion on the edges of needlelike α_s phase, and promotes the passivation of the tips of acicular α_s and the spheroidization [36–38]. The combination of thermal and non-thermal effects of EST leads to the transformation of acicular α_s to β phase (shown in Fig. 3(b)). While further increasing the EST time, the temperature rises sharply in a short time, when the specimen is cooled down in the air, massive needlelike α_M precipitate in the α_p phase in Fig. 3(c). Increasing the EST time to 0.06 s, the temperature exceeds that of the β phase transition temperature in a short time, a large number of finer needlelike α_M are precipitated in both α_p and β phase (shown in Fig. 3(d)).

Table 2
Statistics of the average hardness.

Specimen number	Average hardness of area M (HV)	Average hardness of specimen (HV)
No.0	359 ± 8.7	358 ± 8.7
No.2	347 ± 12.5	350 ± 8.9
No.3	356 ± 9.3	353 ± 10.1
No.4	319 ± 7.0	328 ± 11.6
No.5	368 ± 5.5	369 ± 12.2
No.6	398 ± 5.7	396 ± 13.6

3.2. Compressive mechanical properties

The compressive true stress – true strain curves of the specimens are shown in Fig. 4. The yield strength of the specimens before EST is

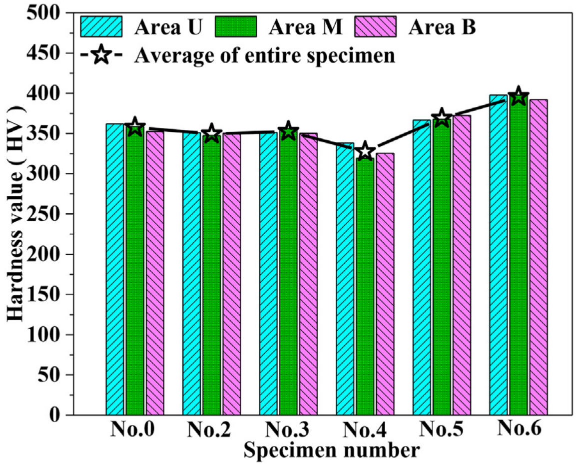

Fig. 7. Average hardness of specimens No.0, No.2, No.3, No.4, No.5 and No.6.

959 MPa, and the fracture strain is 39.1%. The yield strength of No. 2 and No. 3 are not apparently changed. After EST of 0.04 s, the yield strength is significantly reduced to 797 MPa. But with the increase in EST time further, the yield strength of specimens increases to 1036 MPa and 1265 MPa for No. 5 and No. 6, respectively. The decrease in yield strength in No.4 results from the phase transition from acicular α_s to β phase, and the obvious increment in yield strength in No.6 is ascribed to the precipitation of fine needlelike α_M.

From the phase constitution of specimens shown in Fig. 2, one can find that the phase transitions are not evident after EST of 0.02 s and 0.03 s, therefore the yield strength has not shown obvious variation. When the EST time is increased to 0.04 s, as shown in Fig. 2(d) and (d1), the acicular α_s phase transforms into β phase, and the jagged primary α_p/β interfaces begin to become smooth compared to No.0 (Fig. 2 (a) and (a1)). Furthermore, the critical stress for the sliding of grain boundary is reduced, the specimen is prone to be compressed and the yield strength declines. After EST by 0.05 s and 0.06 s, a lot of very fine needlelike α_M precipitate in the α_p phase area are shown in Fig. 2(e), (e1) and (f), (f1). The fine and homogeneous needlelike α_M martensite in No. 6 plays a role of dispersion strengthening in the material, which enhances the yield strength of the specimens No.5 and No.6 after EST.

As shown in Fig. 5, the fracture directions of all specimens present an angle of 45^o along the central axis after compression. The compressive fracture is mainly composed of two typical fractures modes, the plastic fracture and the brittle fracture, which are shown in No. 0 in Fig. 5(a). In the plastic fracture, a large number of dimples are piled up, and in the brittle fracture, a smooth fluvial shape appears. After EST by 0.02 s and 0.03 s, one can find that the areas of smooth fluvial shape decrease (in Fig. 5(b) and (c)), the areas of dimple increase and the size of the dimple becomes larger compared to No. 0, which implies that the plastic fracture is dominant in these samples after EST. The slight reduction in yield strength in No. 2 and No. 3 verifies the variation in fracture mode, and this is attributed to the weakening of the dispersion strengthening of the acicular α_s phase after EST. The area of smooth fluvial shape in No. 3 is smaller than that in No. 2, and the dimple size becomes larger, indicating that the specimen of No. 3 shows the better plasticity and lower yield strength.

With the increase in the EST time, the acicular α_s phase is transformed to β in No. 4 at high temperature. The jagged morphology of the α_p/β interface becomes smooth significantly, as shown in Fig. 2 (d) and (d1). Normally, the plastic fracture should be dominant with the increase of β phase in No.4, but the brittle fracture is dominant in

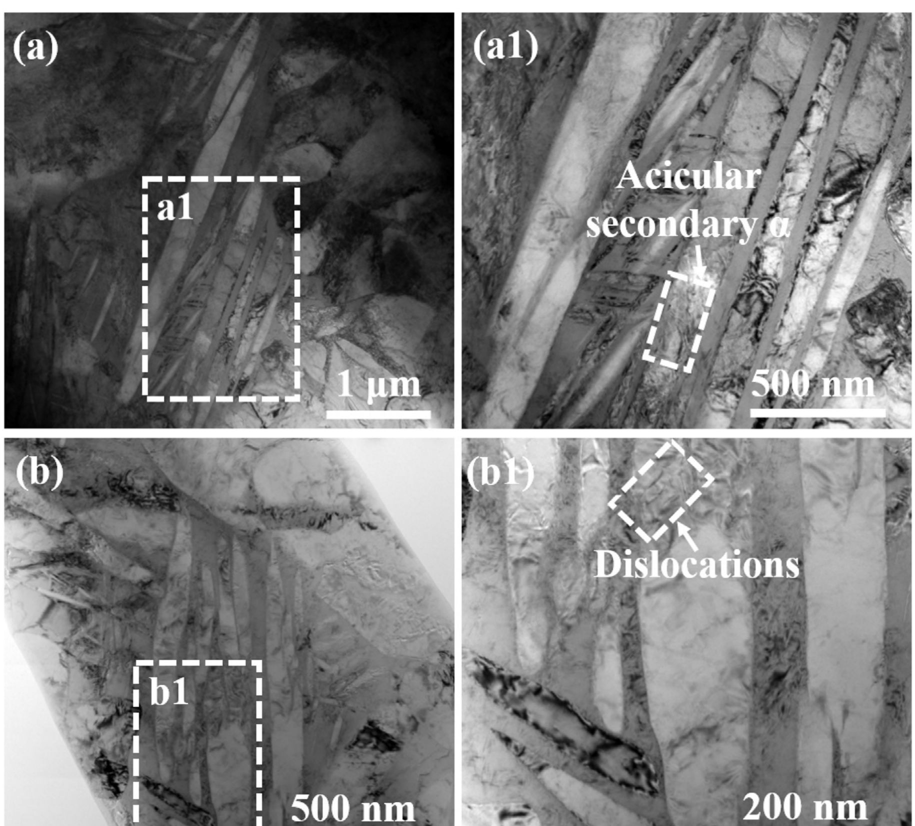

Fig. 8. Bright-field TEM images in the M area of specimen No. 0.

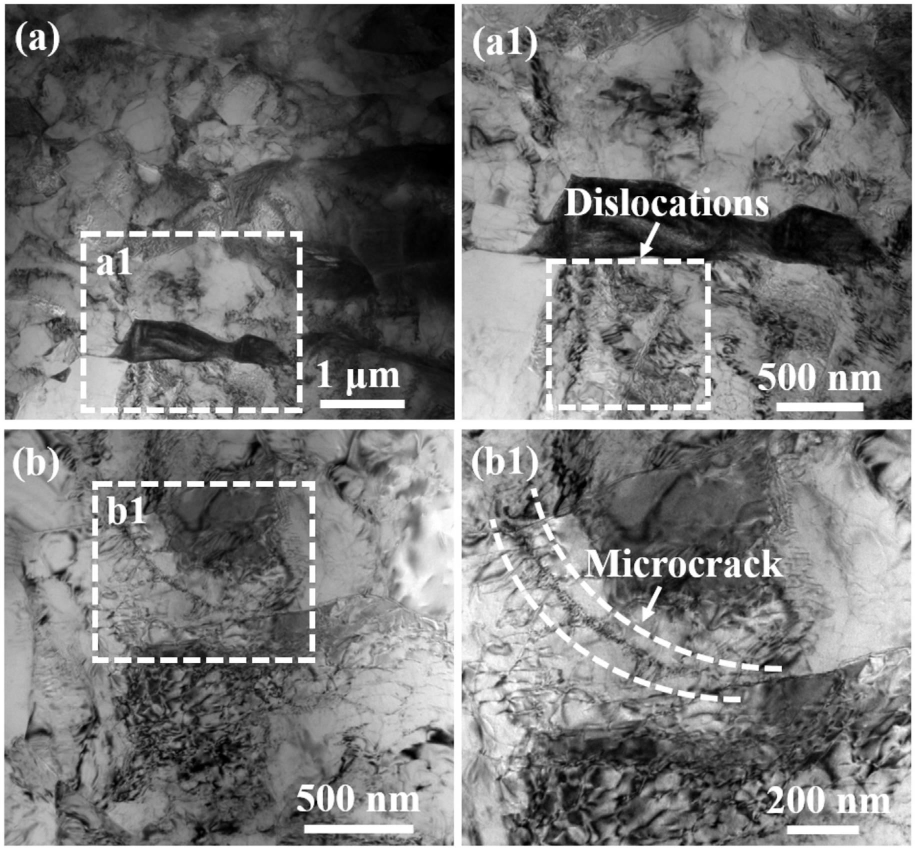

Fig. 9. Bright-field TEM images in the M area of specimen No. 4.

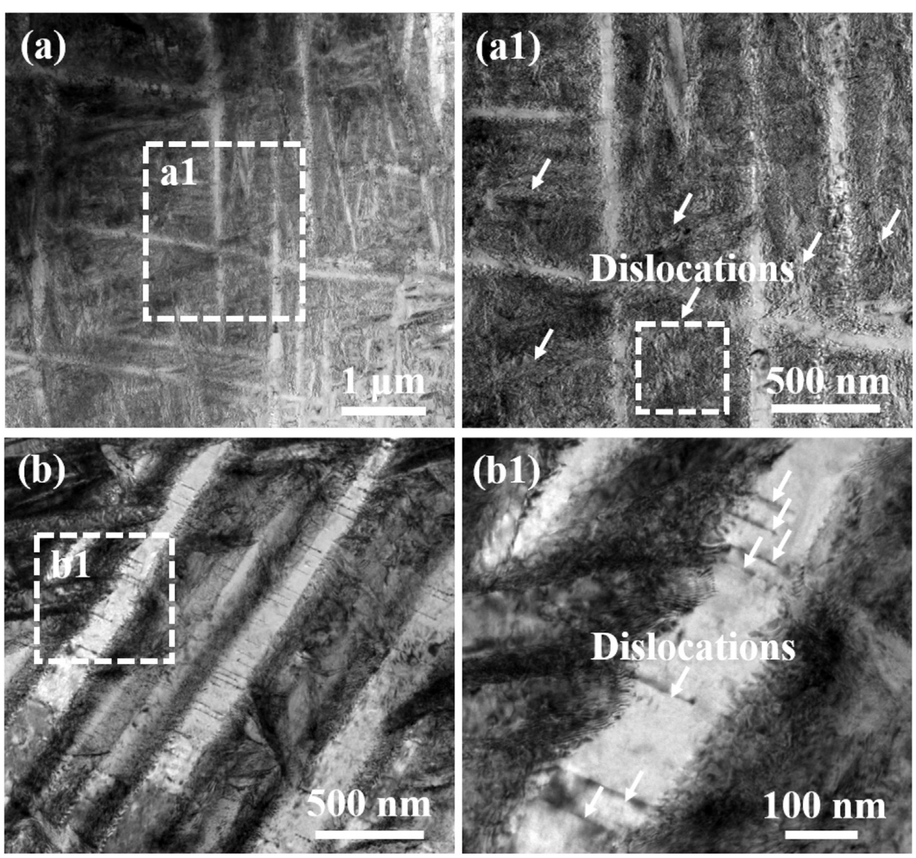

Fig. 10. Bright-field TEM images in the M area of specimen No. 6.

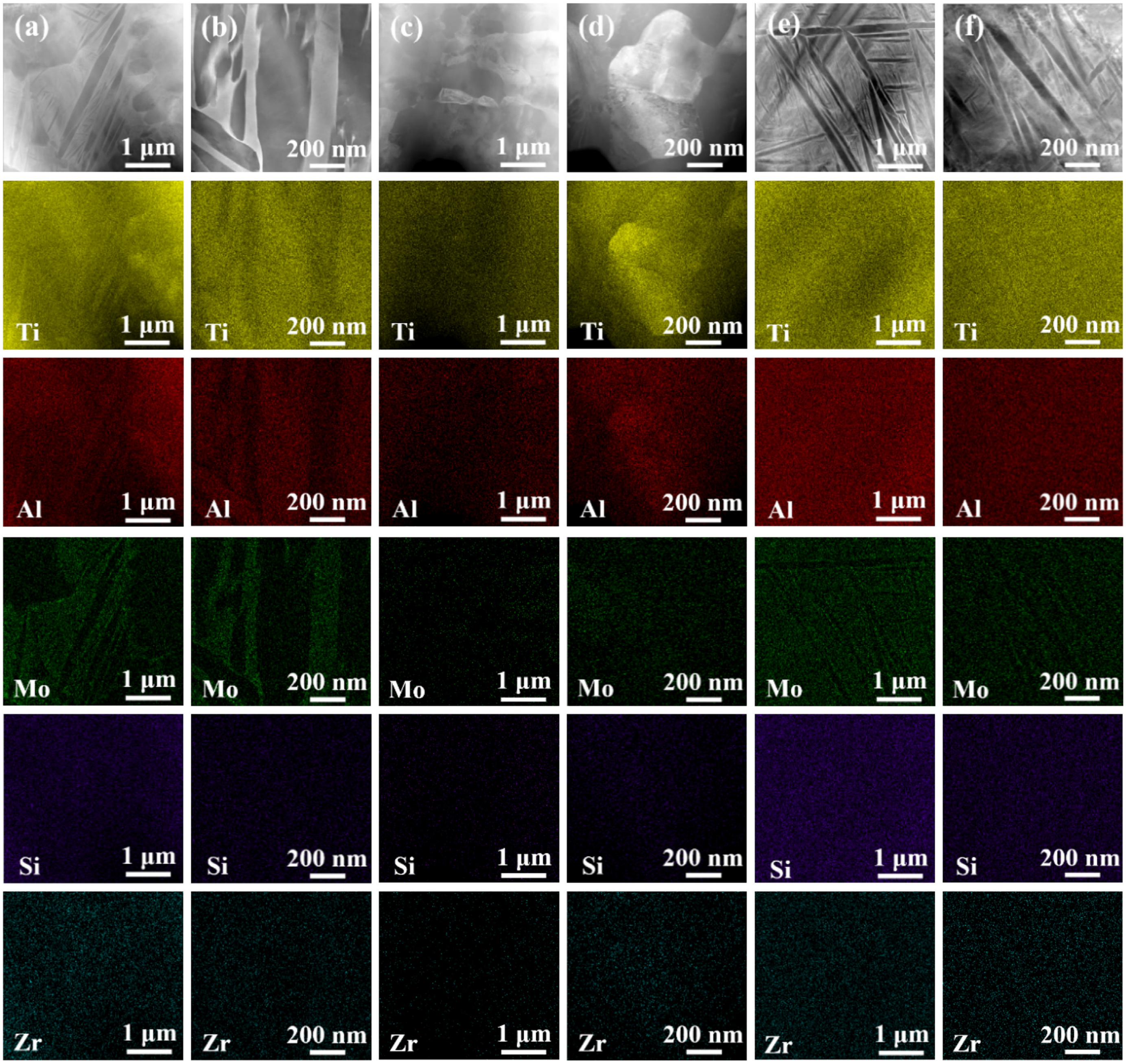

Fig. 11. Element distribution in the M area of specimens No.0, No.4 and No.6; (a) and (b) represent the specimen No. 0, (c) and (d) represent the specimen No. 4, (e) and (f) represent the specimen No. 6.

No.4 from the fracture morphology (shown in Fig. 5(d)), which is caused by more defects in α_s/β interfaces. The fracture mode in No. 4 caused by defects is verified by the TEM results (in Section 3.4). After EST by 0.05 s, the area of smooth fluvial shape increases and the fracture surface is flatter and close to the plane (in Fig. 5(e)). The number of dimples decreases obviously, and the size of dimples also becomes smaller, indicating that the brittle fracture is dominant in No. 5 remarkably. This result is accorded with the improved yield strength of No. 5 (Fig. 4). When the EST time is increased to 0.06 s, the morphology of stacked dimples could not be observed almost in the fracture morphology of No. 6 (in Fig. 5(f)). The fracture morphology of No. 6 is almost the smooth fluvial shape with the extremely small pits, which indicates that the fracture mode of No. 6 is almost the brittle fracture. Therefore, the specimen No. 6 shows the highest yield strength. The enhancement of brittleness fracture in specimens No. 5 and No. 6 is mainly due to the precipitation of needlelike α_M after EST. The variation in fracture mode from the plastic fracture to the brittle fracture is ascribed to the phase transition from the acicular α_s to β and the precipitation of needlelike α_M after EST.

3.3. Hardness variation

The hardness contour of all specimens is shown in Fig. 6. Compared to No. 0, the No. 2 and No. 3 show no obvious variation in hardness, No. 4 shows significant decreased hardness, and No. 5 and No. 6 demonstrate the improved hardness. The statistics of all hardness values are calculated and shown in Table 2 and Fig. 7. The standard deviation of hardness in the M area and the whole specimen are shown in Table 2, the

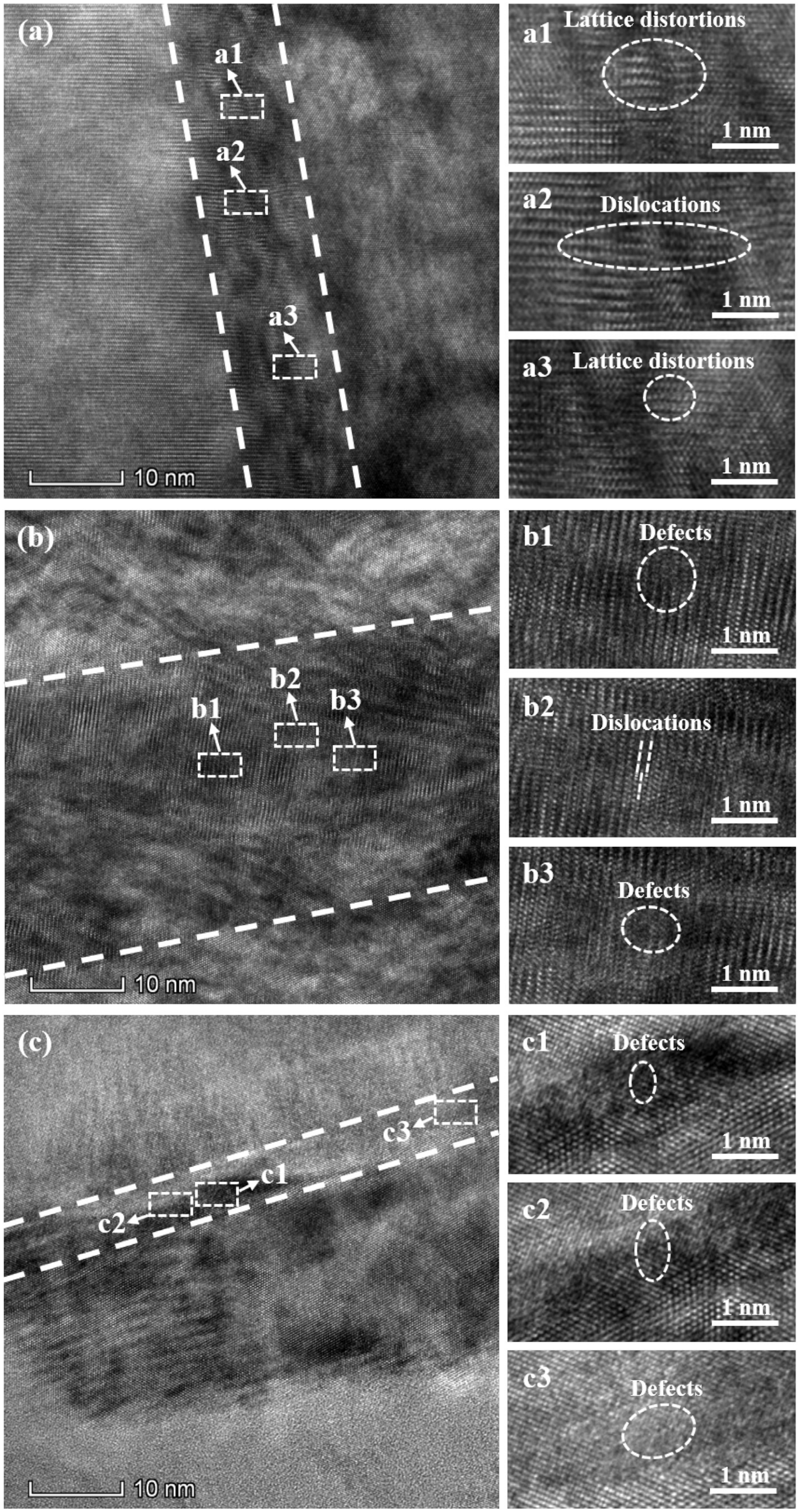

Fig. 12. HRTEM images in the M area of specimens: (a), (b) and (c) represent the specimen No.0, No.4 and No.6 respectively.

standard deviation of hardness in M is smaller than that in the whole specimen, which means that the hardness in M area is distributed uniformly. The three-dimensional contour of the hardness distribution in M shows a good smoothness in Fig. 6.

The average hardness of specimens before and after EST are shown in Fig. 7. The average hardness of No. 0 is 358 HV, those of No. 2 and No. 3 are 350 HV and 353 HV correspondingly, and the variation is not apparent. After EST of 0.04 s, the hardness decreases obviously, and the average value drops to 328 HV. The average hardness of No. 5 and No. 6 are obviously enhanced, corresponding to 369 HV and 396 HV. The variation in hardness is related to the microstructure closely. When the specimens are treated by 0.02 and 0.03 s, the microstructure variation is not obvious compared to No.0, but the slight variation of phase constitution still exists [29], the hardness of No.2 and No.3 show a slight drop compared to No. 0. After EST of 0.04 s, the hardness of No. 4 shows a visible decline, which is attributed from the obvious phase transition of the acicular α_s to β. Moreover, the lattice distortions and dislocation pileups in the grains and the grain boundaries are other reasons for the reduction of hardness in No. 4, and the defects are investigated by TEM in the following section. The hardness of No. 5 and No. 6 increase obviously, which is attributed to the very fine needlelike α_M phase formed inside the specimens after EST by 0.05 and 0.06 s. The precipitation of fine α_M plays a role of dispersion strengthening, so the hardness is significantly enhanced. In addition, the No. 6 has higher hardness than No. 5 due to the strengthening effect of more uniform and finer needlelike α_M.

3.4. Microstructure analysis by TEM

In order to illustrate the mechanism of microstructure variation, TEM characterizations on No. 0, No. 4 and No. 6 were conducted, and the relation between the mechanical properties and the microstructure was revealed. The bright-field TEM images of No. 0 are shown in Fig. 8, the α_s (white) and β (gray) phases shows the clear boundaries (Fig. 8 (a) and (b)). In Fig. 8(a), the acicular α_s phase exists in β phase, which is consistent with the SEM results in Fig. 2(a). A small amount of dislocations is mainly concentrated at the grain boundaries and inside the α_s phase (in Fig. 8(b1)). After EST by 0.04 s, acicular α_s phase is not observed in Fig. 9, because the acicular α_s is almost transformed to β phase. The boundaries of α_s and β phases become ambiguous (in Fig. 9(a) and (b)) compared to the specimen of No. 0. As shown in Fig. 9(a1) and (b1), a large number of dislocations concentrated at the grain boundaries are formed as the dislocation walls in No. 4. The dislocation walls and the potential microcracks formed by the dislocation accumulation in No. 4 are show in Fig. 9(b1). But some grains with few dislocations exist in Fig. 8 (b1), which means that many dislocations are introduced by EST of 0.04 s.

Prolonged the EST time to 0.06 s, different microstructure is observed in Fig. 10(a) and (b). Many fine needlelike α_M interweave with each other to form the weave net structure and a large number of dislocations are filled in the weave net structure. Also, there are many dislocations in the precipitated needlelike α_M (Fig. 10(b1)). Compared with the specimen of No. 4, the needlelike α_M with regular shape precipitates in the microstructure of No. 6, and the fine needlelike α_M precipitates can play a role of dispersion strengthening. Moreover, the increased dislocation density in the fine needlelike α_M further enhances the strength, which is verified by the highest yield strength of No.6 during mechanical testing. However, the specimen of No. 4 has no phase structure similar to No.0 due to incomplete phase transformation, and a large number of dislocations accumulate at the grain boundaries, which deteriorates the strength of grain boundaries and results in the decrease in yield strength. This is consistent with the results of mechanical properties (Fig. 4).

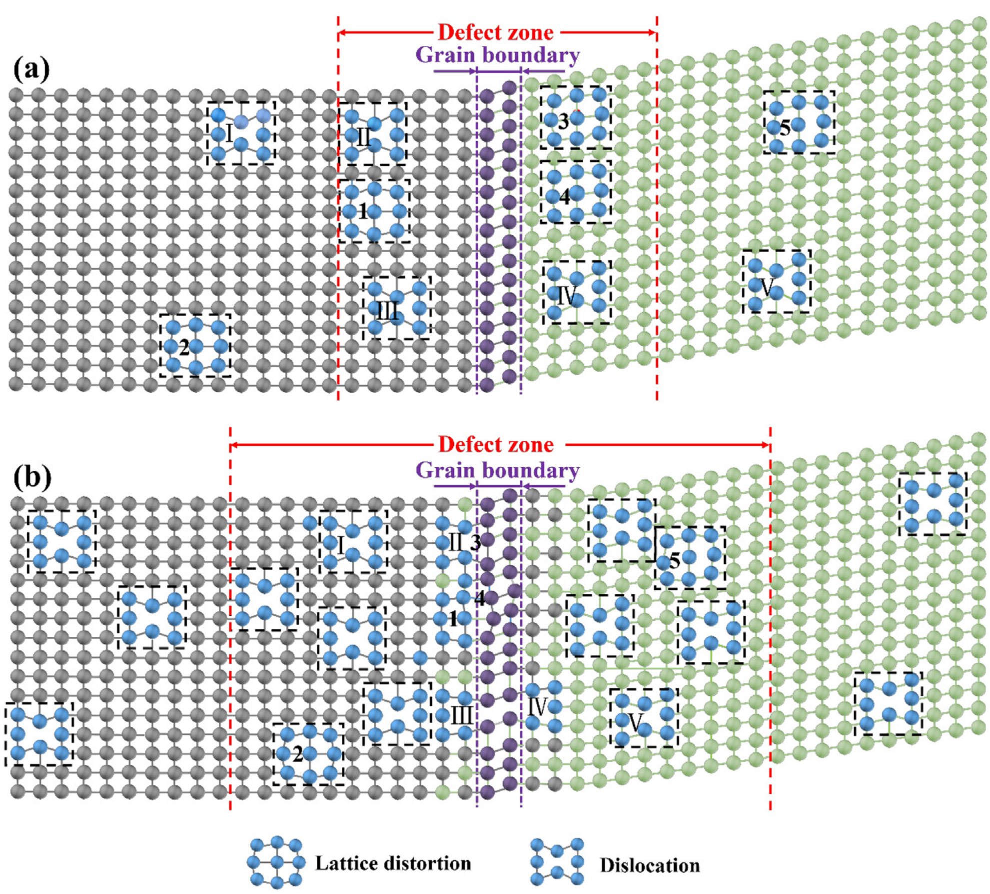

Fig. 13. Schematic of the formation mechanism of defect zone at the grain boundary after EST, (a) represents No. 0, (b) represents No. 4. The labels of 1, 2, 3, 4 and 5 represent the lattice distortions, and the labels of I, II, III, IV and V represent the dislocations.

The element distribution between two phases are shown in Fig. 11 in order to analyze the mechanism of microstructure variation after EST. The chemical elements of TC11 alloy are Ti, Al, Mo, Si and Zr. Among these elements, Al is the element for α stabilization, Mo is the element for β stabilization, and Si and Zr are the neutral elements. Before EST, the distribution of Al and Mo are obvious according to the phase distribution, and the clear interfaces between α_s and β phases can be observed (in Fig. 11(a) and (b)). Moreover, the acicular α_s phase are shown clearly in Fig. 11(a), which is consistent with the SEM results in Fig. 2(a). After EST by 0.04 s, the element distribution of Mo and Al are uniform, and the phase boundaries between α_s and β become ambiguous (in Fig. 11(c) and (d)), which means that the potential element migration occurs between α_s and β. This phenomenon in No. 4 is attributed to the phase transition of the acicular α_s to β after EST of 0.04 s, and the area M (main phase transition area) is characterized by TEM. The phase transition causes the Al and Mo atoms to diffuse between the acicular α_s and β [33]. With the increase of EST time to 0.06 s, the needlelike α_M is precipitated in the whole specimen and the clear boundaries of needlelike α_M can be shown in Fig.11(e) and (f). The Al element is uniformly distributed because the needlelike α_M is precipitated in the whole specimen; but the Mo element is only distributed in the β phase, which indirectly verifies the phase transition and the precipitation of needlelike α_M after EST.

High-resolution TEM (HRTEM) images of grain boundaries in No. 0 and No. 4 are shown in Fig. 12. Usually the atom distribution in the grain boundaries is disordered. In Fig. 12(a), a small number of dislocations (Fig. 12(a2)) and slight lattice distortions (Fig. 12(a1) and (a3)) appear at the grain boundaries of No. 0, which are introduced during the extrusion of the raw materials. There is a defect zone with a width of 11.2 nm at the boundary in No. 0. On two sides of the defect zone at the boundary, the atoms are arranged regularly. After EST by 0.04 s, an increase of the width of the defect zone at the grain boundary in No. 4 to 27.6 nm is observed (in Fig. 12(b)), resulting from the phase transition accompanied by atom migration. In the specimen of No. 4, there are a lot of lattice distortions and dislocation pileups in the area of grain boundaries. Typical edge dislocations can be observed in Fig. 12 (b2). The different dislocations and lattice distortions are mixed to form the defect zone (Fig. 12(b1) and (b3)) which is prone to form the microcracks at the grain boundary during the compression.

After EST by 0.06 s, a reduced width of the defect zone of 5.91 nm at the grain boundary is seen. The formation of defects at grain boundaries in No. 6 may be caused by the fact that more defects are introduced than recovered. The decrease in the width of defect zone at grain boundaries - if statistically significant - reduces the possibility of pileup of dislocations, lattice distortions and other defects to form microcracks, which is beneficial to the mechanical properties. Comparing Fig. 12 (a), (b) and (c) indicates that the arrangement of atoms at grain boundaries is more orderly in No. 6 than that in No. 4 because of the complete phase transition. Because a large number of dislocations are piled up and the defects are formed in No. 4 during compression, many defects are apt to causing the sliding in the grain boundary area, which reduces the yield strength in No. 4 significantly. Due to the different microstructure from No. 4, the fine needlelike martensite in No. 6 interweaves with each other to form the weave net structure, and a large number of dislocations are filled in these weave net structures. Compared with the specimens of No. 0, No. 6 contains much more dislocations and the uniform distribution of needlelike α_M, especially the dislocations cross the needlelike α_M (Fig. 10(a)). Both the dispersion strengthening and the dislocation strengthening of needlelike α_M enhance yield strength. Therefore, No. 6 demonstrates the highest strength among all these specimens.

The schematic of the defect formation near grain boundaries in No. 4 is shown in Fig. 13. The EST promotes the phase transition of the acicular α_s to β phase, which is accompanied by the atom migration. This may produce dislocations and lattice distortions according to the misfit and thermal stresses. Before EST, a small amount of dislocations (I-V) and lattice distortions (1–5) appears near the grain boundaries in No. 0 (Fig. 13(a)). After EST of 0.04 s, the energy of EST is enough to activate the generation of dislocations at the grain boundaries (Fig. 13(b)). Some dislocations (II, III, IV) and lattice distortions (1, 3, 4) near grain boundaries can move to the grain boundaries, which is apt to form the microcracks. However, because the EST time is sub-second, the fast cooling of specimen causes the distant dislocations (I, V) and the distant lattice distortions (2, 5) do not have enough time to completely migrate and rearrange, resulting in the pileup of dislocations and lattice distortions to form the wide defect zone at grain boundaries (Fig. 13(b)). The dislocations and lattice distortions close to grain boundaries widen the width of the defect zone, and the pileup of dislocations and lattice distortions form the dislocation walls or the potential microcracks, which could deteriorate the yield strength. The TEM results are consistent with the microstructure characterization by SEM. The relation between the microstructure and mechanical properties can be illuminated by both SEM and TEM results.

4. Conclusions

The microstructural evolution and the mechanical properties of TC11 alloy before and after EST were investigated, and some important results were obtained.

(1) After EST by 0.04 s, the acicular α_s phase transformed to β phase. As the EST time increased to 0.06 s, the α_p and β phases were not observed, and a large number of fine needlelike α_M were precipitated. Such microstructure evolution was ascribed to the thermal and non-thermal effects.

(2) After EST by 0.04 s, the yield strength was reduced from 959 MPa to 797 MPa, while the EST time increased to 0.06 s, the yield strength was enhanced to 1265 MPa. The average hardness of the specimen first decreased from 358 HV of No. 0 to 328 HV of No. 4, and then increased to 396 HV of No. 6. The variation in mechanical properties resulted from the phase transition of the acicular α_s phase and the dispersion strengthening of the finer needlelike α_M precipitates.

(3) With increasing the EST time from 0.02 s to 0.06 s, the fracture mode of compression gradually transformed from the plastic/brittle fracture to the brittle fracture. The evolution of the fracture mode was related to the microstructure variation. The phase transition and the internal defects of No. 4 also promoted the fracture.

(4) After EST of 0.04 s, a large number of dislocations and lattice distortions piled up at the grain boundaries to form the defects and the potential microcracks in No. 4, which widened the defect zone at the grain boundaries. The defects and the potential microcracks deteriorated the yield strength of No. 4 during compression.

(5) After EST of 0.06 s, the fine needlelike α_M precipitates were interwoven with each other to form the weave net structures, and a large number of dislocations were uniformly filled in these weave net structures. Both the dispersion strengthening and the dislocation strengthening of needlelike α_M promoted the increase of yield strength of No. 6.

(6) All results indicated that the EST can change the microstructure and improve the hardness and yield strength of TC11 ally in a very short time, which verifies that the EST can be utilized as a simple, energy-saving and fast method for manipulating the microstructure and tailoring the mechanical properties of titanium alloys.

Data availability

The raw/processed data required to reproduce these findings cannot be shared at this time as the data also forms part of an ongoing study.

Declaration of Competing Interest

The authors declare that they have no known competing financial interests or personal relationships that could have appeared to influence the work reported in this paper.

Acknowledgements

This work was financial supported by National Natural Science Foundation of China (Grant No. 51901165, No. 51975441, No. 51961125103), Fundamental Research Funds for the Central Universities (WUT 2018IVA063, WUT 2018IVA064), "Chu Tian Scholar" project of Hubei Province (CTXZ2017-05), the 111 Project (B17034), Fundamental Research Funds for the Central Universities (205217017), and Innovative Research Team Development Program of Ministry of Education of China (IRT_17R83). The TEM work was performed at the Nanostructure Research Center (NRC), which is supported by the Fundamental Research Funds for the Center Universities (WUT: 2019Ш012GX), the State Key Laboratory of Advanced Technology for Materails Synthesis and Processing, and the State Key Laboratory of Silicate Materails for Architectures (all of the laboratories are at Wuhan University of Technology).

References

[1] K. Leśniak-Ziółkowska, M. Śmiga-Matuszowicz, A. Blacha-Grzechnik, S. Student, M. Brzychczy-Włoch, M. Krok-Borkowicz, E. Pamuła, W. Simka, A. Kazek-Kęsik, Antibacterial and cytocompatible coatings based on poly(adipic anhydride) for a Ti alloy surface, Bioact. Mater. 5 (3) (2020) 709–720.
[2] A. Kazek-Kęsik, A. Nosol, J. Płonka, M. Śmiga-Matuszowicz, S. Student, M. Brzychczy-Włoch, M. Krok-Borkowicz, E. Pamuła, W. Simka, Physico-chemical and biological evaluation of doxycycline loaded into hybrid oxide-polymer layer on Ti–Mo alloy, Bioact. Mater. 5 (3) (2020) 553–563.
[3] X. Wen, M. Wan, C. Huang, Y. Tan, M. Lei, Y. Liang, X. Cai, Effect of microstructure on tensile properties, impact toughness and fracture toughness of TC21 alloy, Mater. Design 180 (2019) 107898.
[4] S. Ozan, J. Lin, W. Weng, Y. Zhang, Y. Li, C. Wen, Effect of thermomechanical treatment on the mechanical and microstructural evolution of a β-type Ti-40.7Zr–24.8Nb alloy, Bioact. Mater. 4 (2019) 303–311.
[5] H. Li, Y. Ma, B. Xu, D. Bridges, L. Zhang, Z. Feng, A. Hu, Laser welding of Ti6Al4V assisted with nanostructured Ni/Al reactive multilayer films, Mater. Design 181 (2019) 108097.
[6] M.B. Sedelnikova, E.G. Komarova, Y.P. Sharkeev, T.V. Tolkacheva, I.A. Khlusov, L.S. Litvinova, K.A. Yurova, V.V. Shupletsova, Comparative investigations of structure and properties of micro-arc wollastonite-calcium phosphate coatings on titanium and zirconium-niobium alloy, Bioact. Mater. 2 (3) (2017) 177–184.
[7] S. Liu, J. Liu, L. Wang, R.L. Ma, Y. Zhong, W. Lu, L. Zhang, Superelastic behavior of in-situ eutectic-reaction manufactured high strength 3D porous NiTi-Nb scaffold, Scr. Mater. 181 (2020) 121–126.
[8] L. Wang, L. Xie, P. Shen, Q. Fan, W. Wang, K. Wang, W. Lu, L. Hua, L.-C. Zhang, Surface microstructure and mechanical properties of Ti-6Al-4V/Ag nanocomposite prepared by FSP, Mater. Charact. 153 (2019) 175–183.
[9] L. Xie, L. Wang, K. Wang, G. Yin, Y. Fu, D. Zhang, W. Lu, L. Hua, L.-C. Zhang, TEM characterization on microstructure of Ti–6Al–4V/Ag nanocomposite formed by friction stir processing, Materialia 3 (2018) 139–144.
[10] L. Zhang, L. Chen, A review on biomedical titanium alloys: recent progress and prospect, Adv. Eng. Mater. 21 (4) (2019) 1801215.
[11] L. Zhang, L. Chen, L. Wang, Surface modification of titanium and titanium alloys: technologies, developments, and future interests, Adv. Eng. Mater. 22 (2020) 1901258.
[12] L. Wang, L. Xie, L. Zhang, L. Chen, Z. Ding, Y. Lv, W. Zhang, W. Lu, D. Zhang, Microstructure evolution and superelasticity of layer-like NiTiNb porous metal prepared by eutectic reaction, Acta Mater. 143 (2018) 214–226.
[13] L. Wang, L. Xie, Y. Lv, L. Zhang, L. Chen, Q. Meng, J. Qu, D. Zhang, W. Lu, Microstructure evolution and superelastic behavior in Ti-35Nb-2Ta-3Zr alloy processed by friction stir processing, Acta Mater. 131 (2017) 499–510.
[14] H. Ding, Z. Dai, F. Zhou, G. Zhou, Sliding friction and wear behavior of TC11 in aqueous condition, Wear. 263 (1) (2007) 117–124.
[15] X. Li, G. Lu, W.H. Kwok, A.S.C. Chan, Highly enantioselective alkynylzinc addition to aromatic aldehydes catalyzed by self-assembled titanium catalysts, J. Am. Chem. Soc. 124 (43) (2002) 12636–12637.
[16] P. Zhao, L. Fu, H. Chen, Low cycle fatigue properties of linear friction welded joint of TC11 and TC17 titanium alloys, J. Alloys Compd. 675 (675) (2016) 248–256.
[17] H. Song, S. Zhang, M. Cheng, Subtransus deformation mechanisms of TC11 titanium alloy with lamellar structure, T. Nonferr. Metal Soc. 20 (11) (2010) 2168–2173.
[18] Y.Y. Zong, D. Shan, M. Xu, Y. Lv, Flow softening and microstructural evolution of TC11 titanium alloy during hot deformation, J. Mater. Process. Technol. 209 (4) (2009) 1988–1994.
[19] Z.M. Song, L.M. Lei, B. Zhang, X. Huang, G. Zhang, Microstructure dependent fatigue cracking resistance of Ti-6.5Al-3.5Mo-1.5Zr-0.3Si Alloy, J. Mater. Sci. Technol. 28 (7) (2012) 614–621.
[20] K.M. Ibrahim, A.M.M. Elhakeem, R.N. Elshaer, Microstructure and mechanical properties of cast and heat treated Ti–6.55Al–3.41Mo–1.77Zr alloy, T. Nonferr. Metal. Soc. 23 (12) (2013) 3517–3524.
[21] L.J. Huang, L. Geng, A.B. Li, G.S. Wang, X. Cui, Effects of hot compression and heat treatment on the microstructure and tensile property of Ti–6.5Al–3.5Mo–1.5Zr–0.3Si alloy, Mater. Sci. Eng. A 489 (1) (2008) 330–336.
[22] Y. Gu, F. Zeng, Y. Qi, C. Xia, X. Xiong, Tensile creep behavior of heat-treated TC11 titanium alloy at 450–550 °C, Mater. Sci. Eng. A 575 (2013) 74–85.
[23] F. Wang, D. Qian, L. Hua, H. Mao, L. Xie, Voids healing and carbide refinement of cold rolled M50 bearing steel by electropulsing treatment, Sci. Rep. 9 (1) (2019) 1–7.
[24] M. Gao, G.H. He, F. Yang, J. Guo, Z.X. Yuan, B.L. Zhou, Effect of electric current pulse on tensile strength and elongation of casting ZA27 alloy, Mater. Sci. Eng. A 337 (1) (2002) 110–114.
[25] D. Huo, S. Li, Q. Fan, F. Wang, Effects of electric pulse heat treatment on microstructures and dynamic deformation behaviors of Ti6441 alloys, Mater. Sci. Eng. A 530 (2011) 161–167.
[26] Z. Wang, Y. Zhong, G. Cao, C. Wang, J. Wang, W. Ren, Z. Lei, Z. Ren, Influence of dc electric current on the hardness of thermally aged Cu—Cr—Zr alloy, J. Alloys Compd. 479 (1) (2009) 303–306.
[27] X. Liao, Q. Zhai, J. Luo, W. Chen, Y. Gong, Refining mechanism of the electric current pulse on the solidification structure of pure aluminum, Acta Mater. 55 (9) (2007) 3103–3109.
[28] V.V. Levitin, S.V. Loskutov, The effect of a current pulse on the fatigue of titanium alloy, Solid State Commun. 131 (3) (2004) 181–183.
[29] L. Xie, C. Liu, Y. Song, H. Guo, Z. Wang, L. Hua, L. Wang, L. Zhang, Evaluation of microstructure variation of TC11 alloy after electroshocking treatment, J. Mater. Res. Tech. 9 (2020) 2455–2466.
[30] L. Xie, H. Guo, Y. Song, C. Liu, Z. Wang, L. Hua, L. Wang, L. Zhang, Effects of electroshock treatment on microstructure evolution and texture distribution of near-β titanium alloy manufactured by directed energy deposition, Mater. Charact. 161 (2020) 110137.
[31] W. Wu, Y. Song, Z. Wang, S. Ning, L. Hua, Solid phase transformation of Ti–6.6Al–3.4Mo alloy induced by electroshocking treatment, J. Mater. Sci. 55 (5) (2020) 2245–2255.
[32] X. Song, F. Wang, D. Qian, L. Hua, Tailoring the residual stress and mechanical properties by electroshocking treatment in cold rolled M50 steel, Mater. Sci. Eng. A 780 (2020) 139171.
[33] Z. Fan, J. Jian, Y. Liu, Y. Chen, M. Song, L. Jiao, H. Wang, X. Zhang, In situ studies on superior thermal stability of bulk FeZr nanocomposites, Acta Mater. 101 (2015) 125–135.
[34] H. Conrad, N. Karam, S.L. Mannan, Effect of prior cold work on the influence of electric current pulses on the recrystallization of copper, Scr. Mater. 18 (3) (1984) 275–280.
[35] H. Conrad, Electroplasticity in metals and ceramics, Mater. Sci. Eng. A 287 (2) (2000) 276–287.
[36] J.C. Ho, E.W. Collings, Anomalous electrical resistivity in titanium–molybdenum alloys, Phys. Rev. B 6 (10) (1972) 3727–3738.
[37] C. Ouchi, H. Iizumi, S. Mitao, Effects of ultra-high purification and addition of interstitial elements on properties of pure titanium and titanium alloy, Mater. Sci. Eng. A 243 (1) (1998) 186–195.
[38] S.L. Ames, A.D. Mcquillan, The resistivity-temperature-concentration relationships in the system niobium-titanium, Acta Metall. 2 (6) (1954) 831–836.